



T4F³: temperature for fused filament fabrication

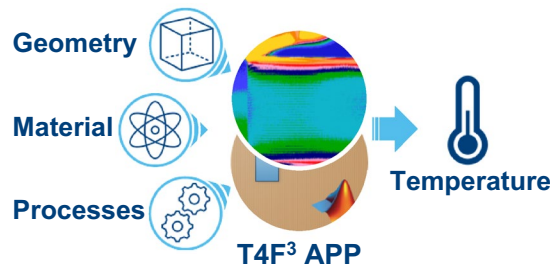
Jie Zhang¹ · Brecht Van Hooreweder² · Eleonora Ferraris¹

Received: 22 July 2021 / Accepted: 24 January 2022 / Published online: 9 March 2022
© The Author(s) 2022

Abstract

Temperature fields and their variations in printed parts are the basis for understanding the physical process of fused filament fabrication (FFF). However, reliable temperature data are still rather limited to date. This article presents a three-dimensional transient-state model to simulate the temporal and spatial temperature variations in FFF printed parts. Model variables range from geometry dimensions and (dynamic) material properties to process parameters, covering all important physical phenomena, including conduction anisotropy and radiant heat transfer. The validation of the model is performed against six sets of experimental temperature data obtained with different geometries, machines, materials, processes, temperature measuring methods, etc. Insights in the thermal process are also reported. For example, the heat penetration depth in printing with poly(lactic acid) is limited to 3 mm, and the Biot number intimately characterises the reheating peaks in temporal profiles. This model shows the potential to become a standardised tool to study the thermal characteristics of FFF printed parts. It is made openly available on website <https://iiv.kuleuven.be/onderzoek/aml/technologyoffer>.

Graphic abstract



Keywords Fused filament fabrication (FFF) · Temperature modelling · T4F3 · Heat penetration depth · Heat transfer · Validation

List of symbols

c_p	Isobaric specific heat capacity [J/g/K]	L, W, H	Geometry length, width and height [mm]
h	Convection coefficient [W/m ² /°C]	n	Discrete time index
h_{rad}	Radiant heat transfer coefficient [W/m ² /K]	N	Total element number ($N = N_L N_W N_H$)
\hbar	Layer thickness [μm]	N_L, N_W, N_H	Element number in length, width and height direction
i, j, k	Discrete spatial indexes	q	Directional heat flux [W/m ²]
	Jie Zhang jie.zhang2@kuleuven.be	$\mathbf{r} = (x, y, z)$	Position vector in Cartesian coordinates
	Eleonora Ferraris eleonora.ferraris@kuleuven.be	t	Time [s]
¹	Department of Mechanical Engineering, KU Leuven, Jan Pieter de Nayerlaan 5, 2860 Sint-Katelijne-Waver, Belgium	t_0	Location-specific deposition moment [s]
²	Department of Mechanical Engineering, KU Leuven, Celestijnenlaan 300, 3000 Leuven, Belgium	t_N	Total time in FFF [s] ($t_N = N\Delta t = N_H\Delta\tau$)
		Δt	Time step [s]
		$\delta\tau$	Intra-layer time [s]
		$\Delta\tau$	Inter-layer time [s] ($\Delta\tau = N_L N_W \Delta t$)
		$T = T(\mathbf{r}, t)$	Temperature [°C, K]

$T_{i,j,k}^n$	Discrete temperature in simulation [$^{\circ}\text{C}$, K]
$T_a(z)$	Air (near environment) temperature above the build plate [$^{\circ}\text{C}$]
T_g	Glass transition temperature [$^{\circ}\text{C}$]
T_n	Nozzle temperature [$^{\circ}\text{C}$]
T_p	Plate temperature [$^{\circ}\text{C}$]
T_{∞}	Far environment (room/chamber) temperature [$^{\circ}\text{C}$, K]
v	(Relative) nozzle travelling speed [mm/s]
$\Delta x, \Delta y, \Delta z$	Cuboid voxel element dimension ($\Delta x = v\Delta t$, $\Delta y = \xi\phi$, $\Delta z = \hbar$)
α	Thermal diffusivity [m^2/s]
ε	Emissivity
λ	Thermal conductivity [$\text{W}/\text{m}/^{\circ}\text{C}$]
$\xi\phi$	Strand width [mm]
ρ	Mass density [g/cm^3]
σ	Stefan–Boltzmann constant
ϕ	Nozzle diameter [mm]
$\Omega(t)$	Changing geometry

Abbreviations

ABS	Acrylonitrile butadiene styrene
AM	Additive manufacturing
BAAM	Big area additive manufacturing
BC	Boundary condition
Bi	Biot number, $\text{Bi} = h\hbar/\lambda$
FDM	Finite difference method
FFF	Fused filament fabrication
FOV	Field of view
HME	Hot-melt extrusion
IR	Infra-red
PDE	Partial differential equation
PEKK	Poly(ether-ketone-ketone)
PLA	Poly(lactic acid)

1 Introduction

Fused filament fabrication (FFF) is a popular thermally driven additive manufacturing (AM) technique based on material extrusion. In a typical process, a thermoplastic filament experiences transitions from the glass state to polymer melt in the hot-end. Then, the material is pushed through the nozzle under pressure by the filament itself. The pressure transfer is enabled by the presence of a cooler polymer recirculation region located nearby the neck of the heat breaker, sealing the gap between the filament and the hot-end barrel [1–3]. Afterwards, the material is selectively deposited onto the build plate, and the extrudate solidifies back into the vitreous state as printed parts with cooling. The solidification process primarily determines the bond formation, bond quality and the ultimate integrity of the parts. As a measure of thermal energy, temperature characterises

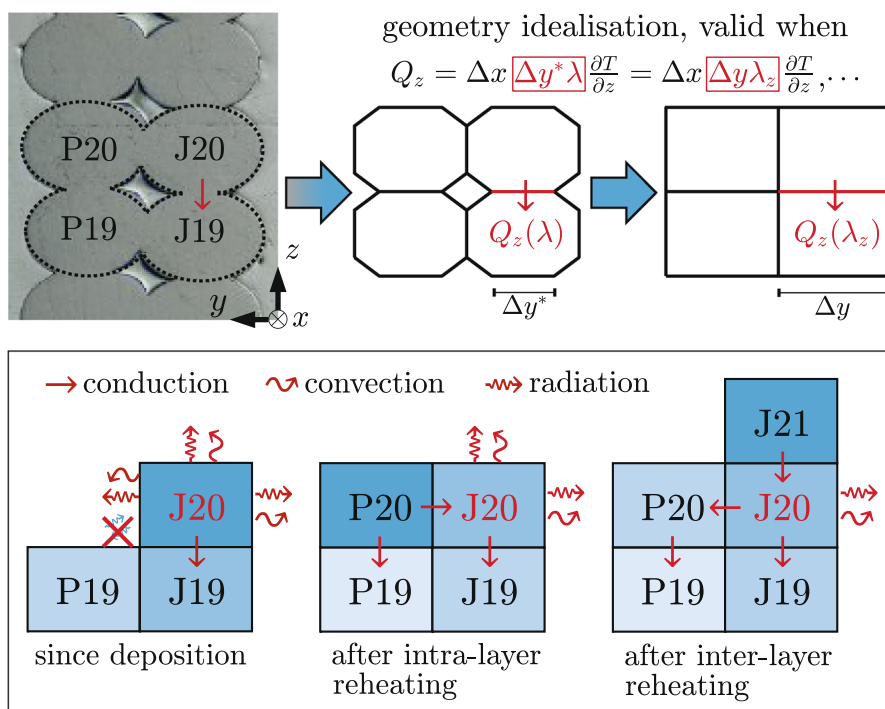
the non-isothermal solidification process [4–6]. As such, insights into the spatial and temporal temperature in the printed parts are essential to understand this AM technology, to tailor the process for optimised material performance.

On the one hand, online temperature monitoring is possible with both contacting (e.g. thermocouple [6, 7], fibre Bragg grating sensor [8]) and non-contacting techniques (e.g. infrared thermography [9, 10]). However, each technique has its limitations, and they can provide only partial information with limited accuracy [11]. On the other hand, numerical modelling provides a fast, economical yet powerful means to probe the temperature variations in FFF parts. The fundamental strategy is to view the additive deposition process as a sequential union of voxel elements for the geometry modelling and then describe pertinent physical phenomena based on the changing geometry [12–14]. As reviewed in Das et al. [15], 28 models were developed to simulate the FFF thermal process between 2015 and 2020. Most of the models for printed parts rely on the element activation function from commercial finite element software to account for the voxel element deposition. Alternatively, the finite difference method (FDM) with adjusted boundaries has also been developed [16, 17]. For most of these models, a single voxel element usually represents the whole cross-section of a deposited strand (track/bead/road), and it is assumed uniform in temperature. Such an assumption is supported by the typical Biot number $\text{Bi} < 0.1$, indicative of a negligible temperature gradient within the strand when the layer thickness is small. Nevertheless, a multi-scaled cross-section and/or bulk geometry model was also discussed [12, 16, 18] and can provide information in multi-resolution at the expense of calculation time and data storage.

Apart from the geometry modelling, the physical process considered reveals more about the nature of this AM technique. Despite some inspiring results from the above models, not all critical physical phenomena were considered. For instance, the air temperature above the plate (*near* environment temperature, associated with the convective heat transfer) was never distinguished from the *far* environment temperature (room/chamber temperature, associated with the radiant heat transfer) [19]. Besides, all currently available models await sufficient experimental validations before being applied to simulate temperature development in printing different 3D geometries with different materials or process parameters. To the best of the authors' knowledge, a comprehensive and sufficiently validated model for temperature distributions and variations in FFF printed parts is still missing.

This article bridges such a gap, offering a validated and open-access numerical model for temperature fields and variations in FFF printed parts. Details of the heat transfer inside the hot-end [2, 20] and during the typical 90° -turn deformation of the extrudate [21] are not included. The

Fig. 1 Top: cross-section of a printed double-wall and its geometry idealisation. The heat transfer is equivalent when the geometrical factors are compensated through the heat flux by adjusted process coefficients and material properties. Bottom: a demonstration of the heat transfer mechanisms of element J20 (deposition sequence: ... , J19, P19, J20, P20, J21, ...)



validation was performed concerning spatial and temporal temperature profiles in FFF with different geometries, machines, materials, processes, temperature measuring methods, etc. Because of the similarities in the fabrication process and heat transfers after the fused deposition, this model can also be applied in a few other thermal energy-driven AM techniques, such as the pellet-based hot-melt extrusion (HME) [22], big area additive manufacturing (BAAM) [23], molten soda-lime glass [24, 25] and molten sugar [26] AM.

2 Numerical model

2.1 Hypotheses

The heat transfer in FFF printed parts is taken as an initial and boundary value problem on a changing domain. Four hypotheses on the physical processes are adopted to model the temperature fields and their variations:

- H1. The FFF process is assumed a sequential deposition of ideal cuboid voxel elements.
- H2. The printed part after the fused deposition is stationary with reference to the build plate.
- H3. The volumetric heat generation by the polymer melt crystallisation is negligible.
- H4. The only significant radiant heat transfer is between the printed parts and the far environment.

H1 assumes FFF printed parts to be compact and porosity-free when the target infill density is 100%. Accordingly, the cross-section of the printed part is idealised as a union of tightly connected rectangles (Fig. 1, top-right). The reality contradicts such idealisation—the real cross-section contains almost unavoidable voids since the building elements, typically of elliptical cross-section, cannot compactly fill in the whole space. On the one hand, those trapped voids will not significantly contribute to the local thermal convection nor thermal radiation between different polymer strands [27]. On the other hand, they can cause anisotropy in thermal conduction due to the uneven bond length, based on which, the (extrinsic) thermal contact resistance can be defined [28, 29]. Ultimately, the voids affect temperature variations in a macroscopic sense. Hence, deviations from the ideal geometry in **H1** can be compensated in the modelling by introducing uncertainties in the heat transfer coefficients and anisotropy in the thermal conductivity ($\lambda_x, \lambda_y, \lambda_z$). As an example, the conductive heat flow Q_z in the model (Fig. 1) can be balanced by defining a reduced thermal conductivity according to the ratio between the real and assumed bond length, i.e. $\lambda_z \equiv \lambda \Delta y^* / \Delta y$. For demonstration purpose, this article only uses homogeneous thermal conductivity ($\lambda_x = \lambda_y = \lambda_z = \lambda$), but the model developed supports anisotropy in the simulation. The authors intend to discuss their impacts and relationship with thermal contact resistance in a separate article.

H2 hypothesises FFF printed parts to be perfectly stationary, with no change in the volume/shape/velocity after the deposition. In particular, the phenomena of bond neck

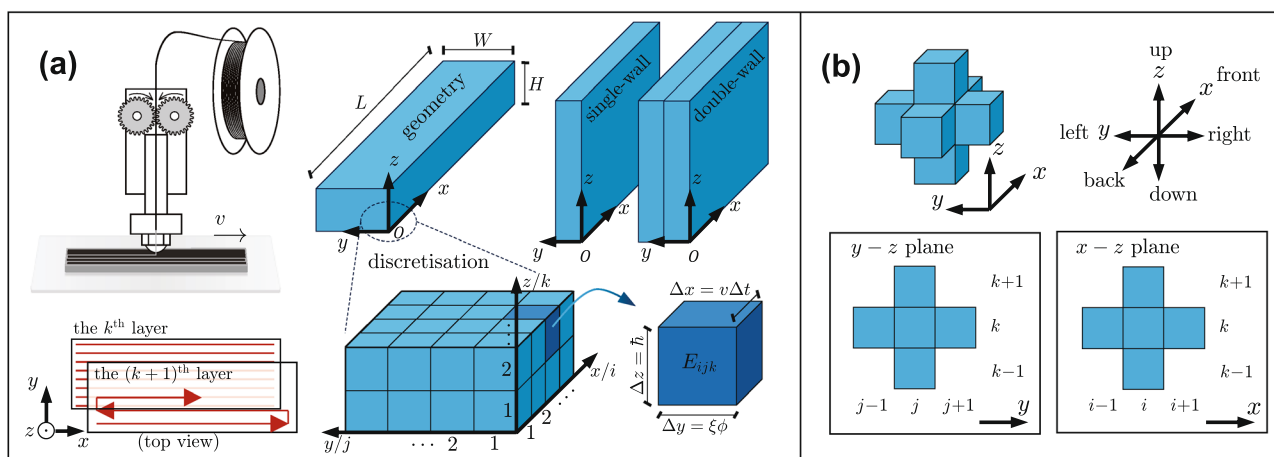


Fig. 2 **a** Diagrams of the FFF machine, process, geometries of interest and the numerical discretisation. **b** The 7-point numerical scheme and the direction convention

growth are neglected considering the limited time duration and volume change. In many cases, the neck growth was not well observed in a dimensional scale comparable to the layer thickness in experiments, e.g. in Fig. 1, the sharp edges of the void kept their shape. Thus, the temperature modelling (energy conservation) decouples from the mass and momentum conservations. In the meantime, the work done by the pressure/viscous/gravitational forces is neglected.

H3 is irrelevant for amorphous polymers; for semi-crystalline polymers, it holds in most cases. For example, neither poly(lactic acid) (PLA) nor poly(ether-ketone-ketone) (PEKK TI-60/40) can considerably crystallise at a cooling rate above 10 °C/min [30, 31]. In contrast, the typical (instantaneous or average) cooling rate in FFF is at least one order of magnitude higher [9, 16]. In addition, PLA has a material melt-crystallisation half time $t_{1/2}$ of about 150 s at the melt-crystallisation temperature $T_{mc} = 100$ °C [32], and the $t_{1/2}$ of PEKK is 12 s in an isotherm at 305 °C [33]. But the duration for those polymers to remain hot enough (e.g. $\geq T_{mc}$) in FFF is usually considerably lower than $t_{1/2}$. However, one needs to treat **H3** with discretion when a heated chamber or a high layer thickness (e.g. ≥ 4 mm, as in BAAM) is used. In either case, the overall cooling rates can be significantly reduced.

H4 simplifies the radiant heat transfer in FFF. The thermal radiation between different locations in the printed part (Fig. 1) is negligible due to their low significance [27]. Meanwhile, the radiant heat transfer between the hot-end and printed part is also ignored for now (despite that Thézé et al. [34] suggested otherwise), since it can only contribute to a reheating in the surface temperature by no more than 5 °C [34, 35]. When there are no additional external/internal heat sources for pre/post-heating [36–39], the only mechanism

retained is the radiant heat transfer between the printed part and the far environment.

2.2 Heat transfer equation

Under hypotheses **H1**, **H2** and **H3**, the governing partial differential equation (PDE) for the temperature field $T = T(\mathbf{r}, t)$ in FFF printed parts takes the form

$$\rho c_p \frac{\partial T}{\partial t} = \nabla \cdot (\lambda \nabla T) = \lambda \left(\frac{\partial^2 T}{\partial x^2} + \frac{\partial^2 T}{\partial y^2} + \frac{\partial^2 T}{\partial z^2} \right), \mathbf{r} = (x, y, z) \in \Omega(t), \quad (1)$$

where the mass density ρ and specific heat capacity c_p can be a pressure/temperature-dependent form such that $\rho = \rho(p, T)$ and $c_p = c_p(p, T)$; t denotes the time, λ the thermal conductivity, $\mathbf{r} = (x, y, z)$ the spatial location, $\nabla T = \left(\frac{\partial T}{\partial x}, \frac{\partial T}{\partial y}, \frac{\partial T}{\partial z} \right)$ the temperature gradient. The changing domain $\Omega(t)$ is specified by the three-dimensional geometry and the building strategy in FFF. Hypothesis **H4** specifies the boundary condition (BC) to the combined type (convection + radiation). Across the boundary, the directional heat flux is

$$q = q_{\text{conv}} + q_{\text{rad}}. \quad (2)$$

2.3 Geometry modelling

The basic geometry of interest is a cuboid of length L (x direction), width W (y direction) and height H (z direction, Fig. 2a). Under hypothesis **H1**, it can be built by depositing ideal voxel elements in a zigzag pattern (a rectilinear infill pattern at 0 ° and an infill density of 100%). The building element has dimensions $\Delta x \times \Delta y \times \Delta z$, where Δy represents the strand width (assumed proportional to the nozzle

diameter ϕ such $\Delta y = \xi\phi$, where ξ is the shape factor [3]); and Δz equals the layer thickness \hat{h} , $\Delta z = \hat{h}$. The product $v\Delta y\Delta z$ provides an estimation of the volume flow rate Q_v in FFF, where v is the nozzle travelling speed relative to the build plate. The choice of the element dimension Δx is arbitrary, but it determines the time step between pseudo-depositions at adjacent locations such that $\Delta t = \Delta x/v$. Accordingly, element numbers in each direction are $N_L = L/\Delta x$, $N_W = W/\Delta y$ and $N_H = H/\Delta z$. The total element number adds up to $N = N_L N_W N_H$. The inter-layer time $\Delta\tau$, indicating the time required to print one layer, can be determined by $\Delta\tau = N_L N_W \Delta t$.

Voxel elements in FFF are chronologically deposited. Accordingly, each has a unique time index n indicating its birth-moment t_0 ($t_0 \equiv n\Delta t$, $n = 1, 2, \dots, N$). The birth-moment of the last element is denoted by $t_{\text{end}} \equiv N\Delta t (= N_H \Delta\tau)$, which is also the time required to finish the printing. In the meanwhile, every element also has a set of unique spatial indexes (i, j, k) ¹ describing its position $\mathbf{r} = (i\Delta x, j\Delta y, k\Delta z)$, ($i = 1, 2, \dots, N_L$; $j = 1, 2, \dots, N_W$; $k = 1, 2, \dots, N_H$). Given the specific zigzag travelling path, a bijection exists between indexes (i, j, k) and n [16]. These voxel elements are symbolically denoted by E_{ijk} , and the FFF building process is essentially a sequential union $\bigcup E_{ijk}$. For each element E_{ijk} , its temperature is assumed uniform within its volume (typically, the Biot number $Bi < 0.1$) and thus denoted by $T_{ijk}^{n\Delta t}$ (or simply T_{ijk}^n)² at the discrete time $n\Delta t$. The time index n here should be higher than or at least equal to the birth-moment index uniquely determined by its spatial indexes (if not, it means that the element has not been deposited yet). n can go beyond N , indicating that FFF is finished, but the heat transfer continues. For the sake of discussion, six directions are defined with respect to the axis orientations: front–positive x ; back–negative x ; left–positive y ; right–negative y ; up–positive z ; down–negative z , as shown in Fig. 2b.

Two special geometries are introduced: double-wall ($N_W = 2$) and single-wall ($N_W = 1$, Fig. 2a). Their temperature variations can be effectively monitored, as demonstrated in [9, 10], respectively. For both geometries, the inter-layer reheating is an important heat transfer characteristic; for the double-wall, the intra-layer reheating can also be well observed. Temperature information in these geometries is representative of printing other geometries as well. When depositing the first perimeter on a new layer in *an arbitrary geometry* and before any intra-layer or inter-layer reheating, the conductive heat transfer takes place only in the

downwards direction in the plane perpendicular to the velocity vector (as anywhere in the single-wall or the right track of the double-wall, e.g. J20 in Fig. 1). When depositing at any locations other than the first deposited perimeter, the conductive heat transfer typically occurs in two directions (downwards and left/right), as represented by the second deposited (left) track of the double-wall (e.g. P20 in Fig. 1). Although reheatings upon thermal contact may bring up the temperature above the material glass transition temperature T_g , its contribution to bond formation can be negligible [4]. Therefore, the temperature information in the double-wall can shed light on the bond formation in printing bulky geometries, as long as the intra-layer and inter-layer times are comparable for different locations of interest.

2.4 The numerical scheme

The finite difference method (FDM, [40]) was adopted to discretise the governing Eq. (1) into

$$\frac{T_{ijk}^{n+1} - T_{ijk}^n}{\Delta t} = \alpha \left(\frac{T_{i+1..}^n - 2T_{i..}^n + T_{i-1..}^n}{\Delta x^2} + \frac{T_{..j+1..}^n - 2T_{..j..}^n + T_{..j-1..}^n}{\Delta y^2} + \frac{T_{..k+1}^n - 2T_{..k}^n + T_{..k-1}^n}{\Delta z^2} \right), \tag{3}$$

where $\alpha = \lambda/(\rho c_p)$ denotes the thermal diffusivity, and T_{ijk}^n the element temperature in position $(i\Delta x, j\Delta y, k\Delta z)$ at $n\Delta t$. The complete form of $T_{i+1..}^n$ is $T_{i+1,j,k}^n$, where the dots ‘.’ indicate the positions of trivial spatial indexes. The truncation error on the right-hand side of Eq. (3) is of $O(\Delta x^2 + \Delta y^2 + \Delta z^2)$. The only unknown T_{ijk}^{n+1} for the next moment can be expressed as a linear combination of the temperature of 6 neighbour elements and itself (Fig. 2b) at the current moment. Hence, Eq. (3) is also referred to as a 7-point scheme. This linear operation can be represented by a tri-diagonal block matrix [16] or more conveniently by a linear operator \mathcal{F} such that

$$T_{ijk}^{n+1} = \mathcal{F} \left(T_{ijk}^n, T_{i\pm 1..}^n, T_{j\pm 1..}^n, T_{..z\pm 1}^n \right). \tag{4}$$

A sufficient condition for a stable 7-point scheme for elements away from the boundaries requires

$$\alpha\Delta t \left(\frac{1}{\Delta x^2} + \frac{1}{\Delta y^2} + \frac{1}{\Delta z^2} \right) \leq 0.5. \tag{5}$$

Since $\Delta t = \Delta x/v$, setting $\Delta x = [(\Delta y)^{-2} + (\Delta z)^{-2}]^{1/2}$ can deliver a most probable stable scheme. In hundreds of simulations already performed, the scheme stability was well observed. In case of instability, the inter-layer time similarity rule [3] can be applied to simultaneously scale up the part length and travelling speed so that the time step in Eq. (5)

¹ The commas between the spatial indexes can be omitted if no confusion arises.

² The superscript $n\Delta t$ or n hereby indicates the time, not the power index.

can guarantee the inequality. Practical tips on the scheme stability are also available in [41].

The initial condition is given by the temperature of every element at its deposition as

$$T_{ijk}^{t_0} = T_i = T_n,$$

where T_i is the actual polymer temperature at the nozzle outlet, and it is assumed to be equal to the nominal nozzle temperature T_n in the stable filament feed region [3]. It is noteworthy that T_i can greatly deviate from T_n (up to 30 °C [20, 42]) at high volume flow rates when the heating power of the hot-end lags behind the polymer melt flow.

The main difficulty in applying Eq. (4) in the calculation is the appearance and disappearance of the boundaries, which originates from the additive nature of FFF. Consequently, the neighbours of E_{ijk} may not have been deposited at a specific moment or might never exist (e.g. element J20 does not have the neighbour P20 before its intra-layer reheating, Fig. 1). This consequence requires boundary condition Eq. (2) to determine the temperature of those *pseudo-neighbours*.

2.5 Boundary condition treatment

For an element surface having an outward normal $e_x = [1, 0, 0]$, the BC gives a constant heat flux across the boundary, equating that by thermal conduction,

$$-\lambda \nabla T \cdot e_x = h(T - T_a) + \varepsilon \sigma (T^4 - T_\infty^4), \tag{6}$$

where h denotes the convective heat transfer coefficient; ε the whole spectrum hemi-spherical material emissivity; σ the Stefan–Boltzmann constant ($5.670 \times 10^{-8} \text{ W/m}^2/\text{K}^4$); T_∞ the far environment (room/chamber) temperature; and T_a the air temperature above the build/heat plate. T_a depends on the vertical height z and decays exponentially from the plate temperature T_p towards T_∞ by a characteristic dimension l_c such that

$$T_a = T_a(z) = (T_p - T_\infty)e^{-\frac{z}{l_c}} + T_\infty. \tag{7}$$

Reference [19] provides more details for Eq. (7). For a parallel surface but negatively oriented (outward normal $e_{-x} = [-1, 0, 0]$), the BC gives

$$-\lambda \nabla T \cdot e_{-x} = h(T - T_a) + \varepsilon \sigma (T^4 - T_\infty^4). \tag{8}$$

In the context of the FDM, Eq. (6) is discretised by a forward scheme [40] into

$$\frac{T_{i+1..}^n - T_{ijk}^n}{\Delta x} = \frac{1}{\lambda} \left[h(T_a - T_{ijk}^n) + \varepsilon \sigma (T_\infty^4 - (T_{ijk}^n)^4) \right].$$

By rearranging,

$$T_{i+1..}^n = T_{ijk}^n + \frac{\Delta x}{\lambda} \left[h(T_a - T_{ijk}^n) + \varepsilon \sigma (T_\infty^4 - (T_{ijk}^n)^4) \right]. \tag{9}$$

Equation (9) is already an iteration-ready form for the calculation. By defining the local radiant heat transfer coefficient $h_{\text{rad}}(T_{ijk}^n) \equiv \varepsilon \sigma [(T_{ijk}^n)^2 + T_\infty^2] (T_{ijk}^n + T_\infty)$, and subsequently, $h_{\text{eff}} \equiv h + h_{\text{rad}}$, Eq. (9) is neatly rearranged into

$$T_{i+1..}^n = T_{ijk}^n + \frac{\Delta x h_{\text{eff}}}{\lambda} (T_\infty - T_{ijk}^n),$$

assuming that the air temperature equals the far environment temperature, i.e. $T_a(z) = T_\infty$ ³. Recalling the direction convention in Fig. 2b, the unknown neighbour temperature is given by

$$T_{\text{front}}^n \equiv T_{i+1..}^n = \left(1 - \frac{\Delta x h_{\text{eff}}}{\lambda} \right) T_{ijk}^n + \frac{\Delta x}{\lambda} h_{\text{eff}} T_\infty. \tag{10}$$

Similarly, Eq. (8) is discretised by a backward scheme [40],

$$\frac{T_{ijk}^n - T_{i-1..}^n}{\Delta x} = \frac{1}{\lambda} \left[h(T_{ijk}^n - T_a) + \varepsilon \sigma ((T_{ijk}^n)^4 - T_\infty^4) \right],$$

and ultimately rearranged into (counterpart of Eq. (10))

$$T_{\text{back}}^n \equiv T_{i-1..}^n = \left(1 - \frac{\Delta x h_{\text{eff}}}{\lambda} \right) T_{ijk}^n + \frac{\Delta x}{\lambda} h_{\text{eff}} T_\infty. \tag{11}$$

The truncation error in Eqs. (10) and (11) is of the order $O(\Delta x)$, which exceeds that of the PDE by Eq. (3). Hence, to realise better error control, the central difference schemes are applied and deliver

$$\frac{T_{i+1..}^n - T_{i-1..}^n}{2\Delta x} = \frac{h_{\text{eff}}}{\lambda} (T_\infty - T_{ijk}^n)$$

for Eq. (6) and

$$\frac{T_{i+1..}^n - T_{i-1..}^n}{2\Delta x} = \frac{h_{\text{eff}}}{\lambda} (T_{ijk}^n - T_\infty)$$

for Eq. (8). By rearrangement, the counterparts for Eqs. (10) and (11) are

$$T_{\text{front}}^n \equiv T_{i+1..}^n = T_{i-1..}^n - \frac{2\Delta x h_{\text{eff}}}{\lambda} T_{ijk}^n + \frac{2\Delta x h_{\text{eff}}}{\lambda} T_\infty, \tag{12}$$

$$T_{\text{back}}^n \equiv T_{i-1..}^n = T_{i+1..}^n - \frac{2\Delta x h_{\text{eff}}}{\lambda} T_{ijk}^n + \frac{2\Delta x h_{\text{eff}}}{\lambda} T_\infty, \tag{13}$$

³ It is assumed only for the purpose of neat formula demonstrations hereafter. They are strictly distinguished in the model.

```

Algorithm T4F3 main structure
Require: geometry, process, material properties,  $[i, j, k] \leftrightarrow n$ 
Ensure:  $N_H \geq 2$ ,  $T_{i,j,k}^n$  known  $\forall$  existing elements
1: for  $n = 2, 3, \dots, N, \dots$  (at each time step) do
2:   if  $n < N$  (FFF in progress) then
3:     for  $J = 1, 2, \dots, n$  ( $\forall$  existing elements) do
4:        $J \leftrightarrow [i, j, k]$ 
5:       take  $T_{i,j,k}^n$  at the current moment ( $t = n\Delta t$ )
6:       (update material properties if necessary)
7:       take/calculate  $T$  of neighbours  $T_{i\pm 1, \cdot}^n, T_{\cdot, j\pm 1, \cdot}^n, T_{\cdot, \cdot, k\pm 1}^n$ 
         (whether a neighbour element has been deposited?)
8:        $T_{i,j,k}^{n+1} = \mathcal{F}(T_{i,j,k}^n, T_{i\pm 1, \cdot}^n, T_{\cdot, j\pm 1, \cdot}^n, T_{\cdot, \cdot, k\pm 1}^n)$  [Eq.(4)]
9:     new element deposition
10:   else (FFF is finished)
11:     (update process parameters if necessary)
12:     for  $J = 1, 2, \dots, N$  ( $\forall$  elements) do
13:        $J \leftrightarrow [i, j, k]$ 
14:       take  $T_{i,j,k}^n$  at the current moment ( $t = n\Delta t$ )
15:       (update material properties if necessary)
16:       take/calculate  $T$  of neighbours  $T_{i\pm 1, \cdot}^n, T_{\cdot, j\pm 1, \cdot}^n, T_{\cdot, \cdot, k\pm 1}^n$ 
17:        $T_{i,j,k}^{n+1} = \mathcal{F}(T_{i,j,k}^n, T_{i\pm 1, \cdot}^n, T_{\cdot, j\pm 1, \cdot}^n, T_{\cdot, \cdot, k\pm 1}^n)$  [Eq.(4)]
    
```

Fig. 3 The main structure of the T4F³ algorithm

which are also linear combinations of the temperature of the boundary element (T_{ijk}^n), the far environment (T_∞) and the neighbours in the opposite direction ($T_{i\mp 1, \cdot}^n$). The truncation error now is of the order $O(\Delta x^2)$, matching that of the PDE scheme. However, Eqs. (12) and (13) require the temperatures at two physical locations to calculate the temperature of boundary elements. The calculation is not always applicable when a neighbour element has not been deposited yet (e.g. when printing the first strand of a new layer), or when such neighbour element never exists (e.g. when printing a single-wall, Fig. 2a). In those cases, the lower order discretisation by Eqs. (10–11) is the only choice.

The BC of the first layer downwards is of the first type (Dirichlet), and the neighbour temperature is assumed to be equal to the plate temperature T_p : $T_{i,j,0}^n = T_p$. Alternatively, a thermal contact resistance between the parts and build plate may be defined. The schemes for BC at all other surface orientations resemble those for the $\pm x$ directions (Eqs. (10) and (11) for the $O(\Delta x)$ scheme, Eqs. (12) and (13) for the $O(\Delta x^2)$ scheme).

2.6 Pseudocode and software application

The pseudocode in Fig. 3 demonstrates the main algorithm structure of the T4F³ model. The primary difficulty resides in step 7. One needs to judge whether an element within the boundary has been deposited and select which type of BC discretisation scheme for the calculation. Those details are further outlined in Appendix 1—Fig. 13. Executable software packages (Windows APP and Matlab APP) were also developed to allow more user-friendly applications of the

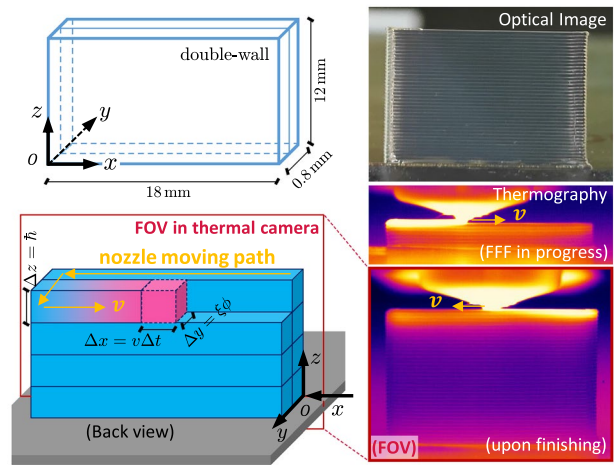


Fig. 4 Schematic of the double-wall geometry in Set 1, the printing process and its optical and thermographic images

model, which are openly available on <https://iiv.kuleuven.be/onderzoek/aml/technologyoffer>. A screenshot of the main graphic user interface is provided in Appendix 2—Fig. 14.

3 Materials and methods

The T4F³ model is first validated through a basic set of experiments (Set 1). This dataset verifies the capability of the model to predict the temporal and spatial temperature profiles of printed parts. Printing experiments were carried out and monitored via thermography. The experimental temperature data were then compared with simulations.

The geometry in Set 1 is a double-wall of dimensions $L \times W \times H = 18 \times 0.8 \times 12$ [mm] (Fig. 4). It was printed on a Prusa i3 MK3, using an E3D V6 brass nozzle with outlet diameter $\phi = 400 \mu\text{m}$ ($= 1/2 W$) and the transparent Prusa PLA filament (diameter 1.75 mm). A thermographic infrared (IR) camera (Optris PI640), working in the spectral range 7.5–13 μm , was employed for the front⁴ view real-time monitoring. The camera worked at a spatial resolution of 31.25 $\mu\text{m}/\text{pixel}$ in a field of view (FOV) of 20.0 \times 15.0 [mm]. The sampling frequency was 32 Hz. The accuracy of the IR camera is $\pm 2^\circ\text{C}$ or $\pm 2\%$, whichever is greater. The temperature at a given location was taken as the mean value of 6×3 pixels, based on an emissivity ϵ of 0.78 for PLA [9]. Table 1 summarises the FFF process parameters and pertaining materials properties. In particular, the part cooling fan was set to its maximum volumetric flow rate of 3.80 cubic

⁴ The directions in the ordinary sense do not follow the conventions in Fig. 2b for the numerical scheme.

Table 1 Details of the temperature monitoring and simulations in FFF and related material extrusion AM processes

	Set 1	Set 2	Set 3	Set 4	Set 5	Set 6
Feature	Desktop FFF machine; low-medium layer thickness		Robot arm-controlled FFF	Chamber temperature controlled; medium layer thickness		High layer thickness and high flow rate
Material	Prusa PLA transparent		Red ColorFabb PLA	ABS	PEKK	CF/ABS
Technology	FFF		FFF on a robot arm	FFF	FFF	BAAM
Data source	Authors	Authors	Authors	[10]	[10]	[23]
Geometry	Double-wall	Double-wall	Single-walled box	Single-wall	Single-wall	Single-wall
Dimension $L \times W \times H$ [mm]	$18 \times 0.8 \times 12$	$18 \times 0.8 \times 12$	$120 \times 1 \times 12$	$60 \times 1.25 \times 50$	$60 \times 2.2 \times 50$	$1542 \times 20 \times 358$
Layer thickness h (Δz) [μm]	300	300	600	800	800	4064
Strand width Δy [μm]	400	400	1000	1250	2200	20,000
Δx [μm]	222.2	439	732	1463	1463	37,610
Travelling speed v [mm/s]	10	5120/60	5	6.741	6.12	39.54
Nozzle temperature T_n [$^{\circ}\text{C}$]	203	203	200	255	356	200
Plate temperature T_p [$^{\circ}\text{C}$]	57.1	57.1	25	100	160	65
Room temperature T_{∞} [$^{\circ}\text{C}$]	21.2	21.2	25	95	139	18
Air temperature $T_a(z)$ [$^{\circ}\text{C}$]	$35.9 e^{-\frac{z}{9.443}} + 21.2$	$35.9 e^{-\frac{z}{9.443}} + 21.2$	25	95	139	$47 e^{-\frac{z}{9.443}} + 18$
Density ρ [g/cm^3]	$\rho = \rho(T)^a$	$\rho = \rho(T)^a$	$\rho = \rho(T)^a$ 1.2261...	1.05	1.14	1.14
Specific heat capacity c_p [$\text{J}/\text{g}/\text{K}$]	$c_p = c_p(T)^a$	$c_p = c_p(T)^a$	$c_p = c_p(T)^a$ 1.8011...	2.1	2.2	1.64
Thermal conductivity λ [$\text{W}/\text{m}/\text{K}$]	0.195	0.195	0.195	0.210.151...	0.510.25 [43]	0.17
Convective coefficient h [$\text{W}/\text{m}^2/\text{K}$]	60	608.5	8.5	308.5	308.5	8.5
Emissivity ϵ	0.78	0.7810	0.78	0.91	0.9410.751...	0.8710
Volume flow rate Q_v [cm^3/h]	4.3	2.218.6/26	11	24	39	1.2×10^4
Inter-layer time $\Delta \tau$ [s]	3.6	7.2/1.8/10.6	24	8.9	9.8	39
Biot number $\text{Bi} = h\bar{h}/\lambda$	0.092	0.092/10.013	0.026	0.12/10.034	0.048/10.014	0.20
Temperature measurement details	Set 1 and Set 2 use the same temperature monitoring setup, as explained in Sect. 3		In line with [3]	A pyrometer (Pyrospot DEP 10 M, DIAS infrared system), working in the spectrum range of 3.7–5.1 μm . Target area 600 μm in diameter. The emissivity was 0.91 for ABS and 0.94 for PEKK	A FLIR A35 thermal camera, working in the spectrum range 7.5–13 μm and sampling frequency 1 Hz. Accuracy: ± 5 $^{\circ}\text{C}$ or $\pm 5\%$	

^aData sources [44, 45]

feet per minute, and the convective heat transfer coefficient h was set at $60 \text{ W}/\text{m}^2/\text{K}$ as in [27].

In addition, five more datasets (Set 2–6) were collected to study the robustness of the model under different experimental conditions, including changes in the processes, materials, part geometries and equipment. These studies focus only on the temporal profiles at selected locations. The experimental details are summarised in Table 1. The features of each dataset are briefly introduced hereby.

The experimental work in Set 2 is constructed as Set 1 except for the nozzle travelling speed. The temporal temperature profiles at the geometry centre (front view) are captured and analysed. The roles of radiant and convective heat

transfer are discussed. Set 3 makes use of an own-developed robot arm assisted FFF experimental setup [3]. A standard E3D V6 hot-end was mounted on a robot arm and controlled for movement. The printing was performed on a non-heated poly(methyl methacrylate) (PMMA) plate covered with paper tape in the open air. The geometry printed was a single-walled box. Set 4 and 5 include experimental data kindly shared by Lepoivre et al. [10], where a heated chamber was used. The heated chamber can effectively reduce the convective heat flux intensity and, ultimately, the overall cooling rate. Besides, the nozzle temperature in Set 5 exceeded 350 $^{\circ}\text{C}$ in printing PEKK. Set 6 includes experimental data kindly shared by Compton et al. [23], where the BAAM

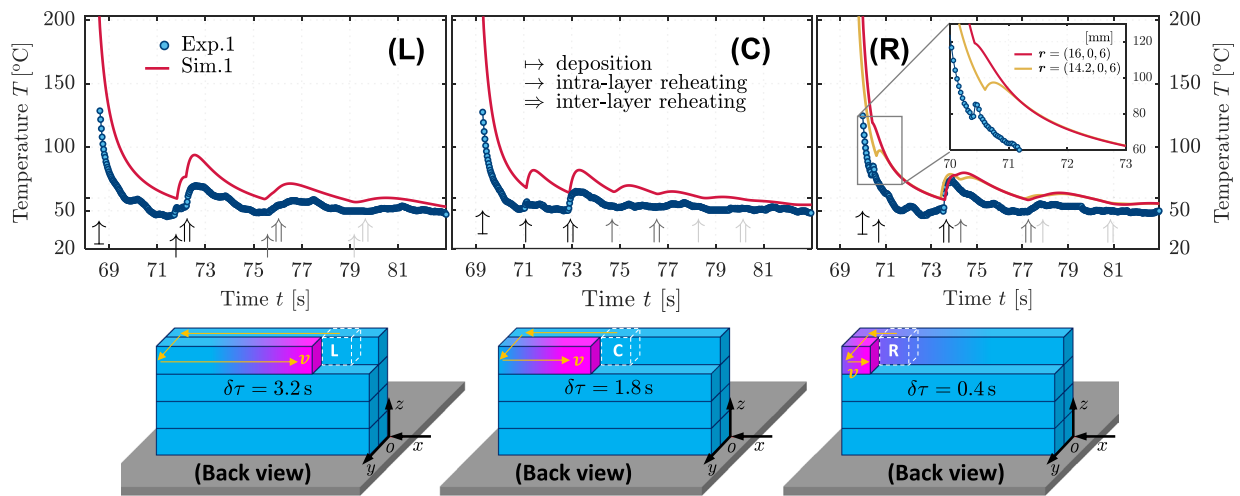


Fig. 5 Experimental and simulation results of temporal temperature profiles at different locations. **L** left side, $\mathbf{r} = (2, 0, 6)$ [mm], intra-layer time $\delta\tau = 3.2$ s; **C** centre, $\mathbf{r} = (9, 0, 6)$ [mm], $\delta\tau = 1.8$ s; **R** right

side, $\mathbf{r} = (16, 0, 6)$ [mm], $\delta\tau = 0.4$ s). The diagrams below show the moment before the intra-layer reheating at each location

system was used for printing. The layer thickness was $10 \times$ higher than the typical values used in FFF desktop printers. As a result, the volume flow rate Q_v exceeded 10^4 cm³/h, which can considerably increase the building efficiency.

4 Results

The model validation against **Set 1** experimental data are discussed with respect to (1) temporal temperature profiles at given locations, (2) temperature fields at different times and, (3) temperature gradient at selected locations and times.

4.1 Temporal temperature profiles

The experimental and simulated temporal temperature profiles at different locations on the 20-th layer in the double-wall are shown in Fig. 5.

Rapid cooling takes place at all three locations right after the deposition, followed by periodic intra-layer and inter-layer reheatings (denoted by \uparrow and $\uparrow\uparrow$, respectively). The intra-layer reheating manifests the thermal conduction between strands on the same layer. Given the dimensions and parameters, the intra-layer time $\delta\tau$ depends on the x coordinates such $\delta\tau = 2(L - x)/v$. At travelling speed $v = 10$ mm/s, the intra-layer reheating (denoted by the first \uparrow from left) takes place 1.8 s after the voxel element deposition at the geometry centre ($\mathbf{r} = (9, 0, 6)$ [mm], Fig. 5C). The inter-layer time $\Delta\tau = 2L/v = 3.6$ s, which doubles the intra-layer time. Thus, intra-layer and inter-layer reheatings are equally spaced but differ in intensity because of different

conduction conditions (e.g. bond length). On the left⁵ side, e.g. at $\mathbf{r} = (2, 0, 6)$ [mm], $\delta\tau$ is comparable to $\Delta\tau$; the peaks due to intra-layer and inter-layer reheatings overlap with each other (Fig. 5L). On the right⁵ side, e.g. at $\mathbf{r} = (16, 0, 6)$ [mm], $\delta\tau \ll \Delta\tau$, the intra-layer reheating takes place right after the deposition. As a result, only a tiny peak/disturbance is observed (Fig. 5R); consequently, the first inter-layer reheating peak overlaps with the *secondary* intra-layer reheating (Fig. 1, P20 \rightarrow (J20&P19) \rightarrow J19). At all locations, reheatings can penetrate through a few layers. However, the deeper they penetrate, the lower their intensities, as suggested by the greyscales of the \uparrow and $\uparrow\uparrow$ arrows in Fig. 5.

From Fig. 5, the model can predict similar temperature patterns in thermography. However, considerable discrepancies are visible between the experimental monitoring and simulations. Particularly, the maximum temperature upon deposition is not correctly captured in the monitoring, possibly due to the thermal reflections in the IR signal transmission. At such a low volume flow rate of 4.3 cm³/h (Table 1), the extrudate temperature is expected to be effectively raised to the nominal nozzle temperature [42, 46]. Thus, the majority of the discrepancy comes from the experimental error *in this specific dataset*. A critical discussion on the possible sources of inaccuracy (such as thermal reflections, sampling frequency) in IR thermography is given in [9]. It awaits dedicated calibrations before accurate temperature data can be extracted from IR monitoring. Furthermore, the intra-layer reheating peak at $\delta\tau = 0.4$ s is not correctly predicted by the model (Fig. 5R); but in the simulation for a next location,

⁵ The “left” and “right” concepts here refer to the front view.

e.g. $\mathbf{r} = (14.2, 0, 6)$ [mm] ($\delta\tau = 0.76$ s), it appears. This observation indicates that the uncertainties in input variables may also contribute to the discrepancy between the experimental and simulation data.

4.2 Temperature fields

A few characteristic times were chosen to examine the capability of the model to predict the temperature fields $T(x, y = 0, z, t)$ of the printed part. The experimental observations are shown on the left side of Fig. 6. Specifically, t_{end} ($= 144$ s) denotes the total time required to print the double-wall in FFF, and $2t_{\text{end}}$ is a typical time indicating the steady state after the printing.

As observed in Fig. 6-left, newly deposited layers remain relatively hot upon finishing ($t = t_{\text{end}}$). The temperature gradient mainly exists in the vertical direction ($|\nabla T| \approx |\partial T/\partial z|$) and directs downwards ($\partial T/\partial z > 0$) for the top 8–12 layers. Recalling the layer thickness $\bar{h} = 300$ μm , the impact reaches roughly 3 mm—a characteristic *heat penetration depth* for PLA. On the contrary, the gradient always directs upwards ($\partial T/\partial z < 0$) for the bottom 8–12 layers above the build plate. These gradients suggest that newly deposited layers have limited influence over the energy equilibrium of the bottom layers, when the nozzle prints the 24-th layers onwards (or the 16-th, as a bolder estimation. See white boxes in Fig. 6). In addition, the energy balance will be locally reached within their above and below 8–12 layers. Such a local equilibrium is almost independent of the printed part height and provides a physical proof of the *active body* concept used by Zhang and Shapiro [17] in their simulations. These observations suggest that a local thermal disturbance exerts only limited influence in space.

On the other hand, the temperature field upon finishing ($t = t_{\text{end}}$) is not symmetric with respect to the plane $x = L/2$. Due to the sequential deposition, the corresponding thermal boundary is asymmetrical in spite of the symmetry in x coordinates. At the steady state (e.g. $t = 2t_{\text{end}}$), the temperature field from the monitoring is neither in perfect symmetry because of some subtle differences in the mesostructures at different locations [9]. These results show that the gradient component $\partial T/\partial x$ exists in printed parts (but not obvious on a colour map of a wide range in thermography), and it sets a reminder that a simplification of the FFF thermal simulation from 3D to 2D or even 1D heat transfer problem may need further discretion.

The simulations in Fig. 6-right capture all characteristics aforementioned, as they can manifest the moving of the active body, the concept of heat penetration depth and the temperature gradients at different times. However, some discrepancies still exist. For example, the temperature fields

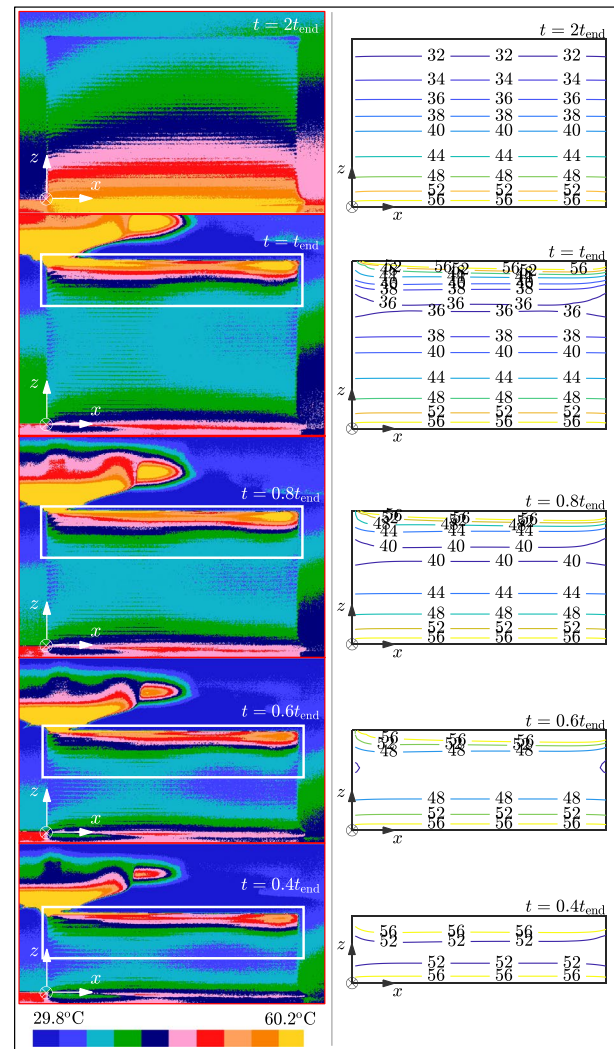


Fig. 6 Temperature fields on the x - z plane at different characteristic times during and after printing. Left: monitoring (white boxes highlighting the top 8–12 layers). Right: simulations with isotherm lines. $t_{\text{end}} = 144$ s

at the steady state ($t = 2t_{\text{end}}$) do not show equally apparent variations along the x axis, indicating the material properties and process parameters may require fine-tuning. Despite so, these results earn more credibility to the T4F³ model.

4.3 More on the temperature gradient

It is clear from Fig. 6 that the temperature gradient component in the x direction is far less significant than that in the z direction, i.e. $|\partial T/\partial x| \ll |\partial T/\partial z|$. Hence $x = L/2$ is fixed, and more results on $T = T(z, t)$ at different times are discussed. Here, t takes different values after the element deposition at $\mathbf{r} = (9, 0, 12)$ [mm] at $t_0 = 141.30$ s. Figure 7 presents corresponding results.

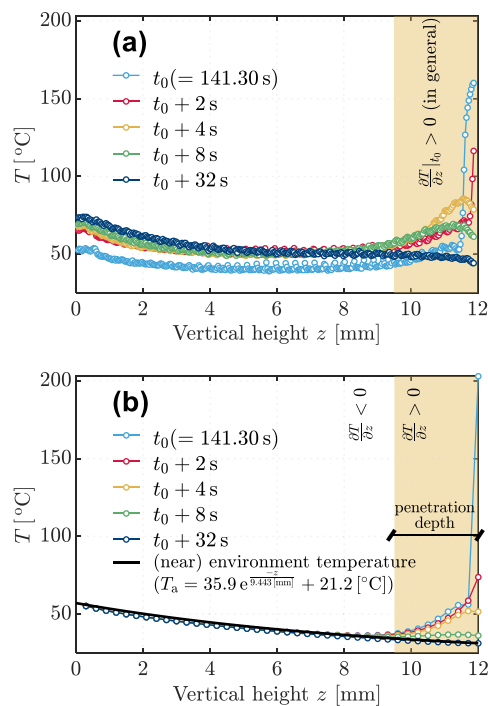


Fig. 7 Temperature dependence on the vertical height. **a** Monitoring. **b** Simulation data

In Fig. 7, the monitoring and simulations can capture similar evolutions of the temperature profiles. Since the deposition at t_0 , considerable temperature gradients exist in the top few layers along the z direction. The maximum gradient component $|\partial T/\partial z|$ reached $920\text{ }^\circ\text{C}/\text{mm}$ from the monitoring; while in the simulation, a maximum $|\partial T/\partial z| = 568\text{ }^\circ\text{C}/\text{mm}$ was predicted. Although the exact value differs, the magnitude matches. Such gradients quickly faded out as a consequence of fast cooling. Eventually, the temperature profile takes the shape of the near environment temperature $T_a(z)$.

As the temperature gradient directs the conductive heat flow, one can observe that most thermal energy flows downwards for the last 8–10 layers ($\partial T/\partial z > 0$ in general). This layer number can also be used to define the heat penetration depth and agrees with the observations in Fig. 6. The heat penetration depth depends on the process, material and, more profoundly, the geometry. The thin double-wall in this dataset will cause energy loss to the environment faster than bulky geometries of smaller specific surface areas. On the bottom layers, temperature gradients had already reached a quasi-steady state at t_0 , suggesting that the penetration depth is limited. The simulations in Fig. 7b can capture the profile evolutions since the deposition. The heat penetration depth

and the eventual shape of the profiles are well demonstrated, showing that the model can reveal temperature gradient information as well.

5 Robustness study and discussions

Another five sets of temperature data were collected (Table 1) to further validate the model and probe its robustness. These data cover different aspects in heat transfers in FFF and similar technology (e.g. BAAM), including different machines, materials, geometries, processes, volume flow rates and temperature measuring methods. Simulations were performed, analysed and compared with experimental monitoring data. They validate the robustness and the applicability of the model to a variety of typical FFF situations and demonstrate the potential of the T4F³ model as a learning and analysing tool for FFF. In each dataset, multiple simulations were performed, and key parameters were varied for comparisons, as summarised in Table 2.

5.1 Set 2 and an example of different processes and the influence of radiation and convection

The experimental and simulation work presented in Set 1 also apply to other FFF situations. Currently, at least 18 variables (part geometry dimensions $L \times W \times H$, nozzle temperature T_n , plate temperature T_p , room/chamber temperature T_∞ , air temperature above the build plate $T_a(z)$, travelling speed v , strand width $\xi\phi$, layer thickness \hat{h} , material density $\rho(p, T)$, specific heat capacity $c_p(p, T)$, thermal conductivity ($\lambda_x, \lambda_y, \lambda_z$), convective coefficient h , emissivity ϵ , and flat nozzle tip width [41]) can be varied in the model while experimentally monitored.

As an example of different processes, data Set 2 was collected, including temporal temperature profiles at different nozzle travelling speeds. The monitoring and simulation details coincide with Set 1 (Table 1). Critical parameters in each subset are summarised in Table 2. In addition to that, the voxel element dimension Δx was increased in the simulations to reduce the storage and calculation time; however, its influence on the result is trivial.

The temporal temperature profiles at the geometry centre in the front view are presented (Fig. 8a). The travelling speeds v were 5 and 20 mm/s in the monitoring (Exp.2-1 and Exp.2-2). The normalised temperature $\frac{T-T_\infty}{\max T-T_\infty}$ was plotted against the normalised time $\frac{t-t_0}{\Delta\tau}$, where t_0 is the respective deposition time at the two speeds ($t_0 = 138.60\text{ s}$ at $v = 5\text{ mm/s}$; $t_0 = 34.65\text{ s}$ at $v = 20\text{ mm/s}$), $\Delta\tau = 2L/v$ the inter-layer time. The rapid cooling after the deposition, intra-layer

Table 2 A summary of non-trivial variables in the simulations

Dataset	Simulations	v [mm/s]	ϵ	h [W/m ² /K]	ρ [g/cm ³]	c_p [J/g/K]	λ [W/m/K]
Set 2	Sim.2-1	5	0.78	60	—*	—	—
	Sim.2-2	20	0.78	60	—	—	—
	Sim.2-3	60	0.78	60	—	—	—
	Sim.2-4	5	0	60	—	—	—
	Sim.2-5	5	0.78	8.5	—	—	—
Set 3	Sim.3-1	—	—	—	$\rho(T)$	$c_p(T)$	—
	Sim.3-2	—	—	—	1.226 (58.11 °C)	1.801 (58.11 °C)	—
	Sim.3-3	—	—	—	1.25 (25 °C)	1.314 (25 °C)	—
Set 4	Sim.4-0	—	0	30	—	—	—
	Sim.4-1	—	0	15	—	—	—
	Sim.4-2	—	0	8.5	—	—	—
	Sim.4-3	—	0.91	8.5	—	—	—
Set 5	Sim.5-0	—	0	30	—	—	0.5
	Sim.5-1	—	0	30	—	—	0.25
	Sim.5-2	—	0	8.5	—	—	0.25
	Sim.5-3	—	0.94	8.5	—	—	0.25
Set 6	Sim.6-0	—	0.87	—	—	—	—
	Sim.6-1	—	0	—	—	—	—

*: “—” indicates trivial variables that are identical within the dataset. They can be found in Table 1

and inter-layer reheatings share similar patterns for both speeds. However, the exact intra-layer and inter-layer times differ, resulting in different reheating moments. In the faster case, both inter-layer and intra-layer time are shorter, inducing higher neighbour temperature upon reheatings. Ultimately, the temperature gradients upon reheatings are smaller, and the reheating peak heights are lower. These thermal characteristics in the monitoring are well reflected in the simulations, suggesting the model can capture the essential heat transfer mechanisms in FFF with different process parameters. However, if the travelling speed further increased to 60 mm/s, the printing showed repeatable failures due to slow cooling. The simulation Sim.2-3 intuitively explains the situation. As an indicator, the temperature upon inter-layer reheating was ~ 160 °C, comparable to the melt temperature of PLA.

Likewise, some discrepancies exist between the monitoring and simulations in Fig. 8a. Apart from the aforementioned errors in the IR camera, the remaining subsection exams the roles of radiant and convective heat transfers in the simulations based on the experimental work at $v = 5$ mm/s.

The significance of radiant heat transfer was investigated with Sim.2-4, which was identical to Sim.2-1 (details in Table 2) except that the material emissivity ϵ was 0. Figure 8b presents corresponding results. Visual inspection shows that the temperature profile is slightly higher than

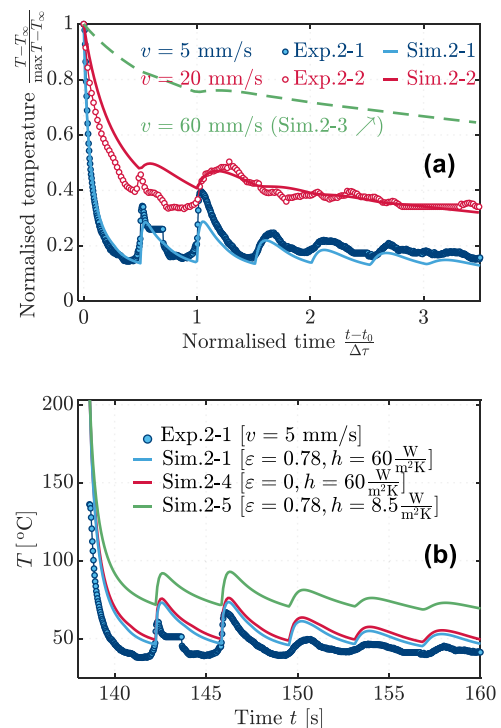


Fig. 8 [Set 2] **a** Temporal temperature profiles at different travelling speeds (location at $\mathbf{r} = (9, 0, 6)$ [mm]). **b** Temporal temperature simulations with different process parameters and material properties

Sim.2-1 when the radiant heat transfer is neglected. To quantify the difference in the two temporal temperature profiles, the $\|\bullet\|_\infty$ norm was applied within $\Delta\tau$ seconds after the deposition:

$$\|\bullet\|_\infty = \max_{t_0 \leq t \leq t_0 + \Delta\tau} \text{abs}(\bullet), \tag{14}$$

where \bullet denotes the difference between any two temporal profiles. By calculation, $\|T_{2.4} - T_{2.1}\|_\infty = 4.1 \text{ }^\circ\text{C}$. Such a difference can be neglected in FFF, suggesting the contribution of radiant heat transfer in the cooling is negligible in this dataset. This suggestion agrees with the conclusion in [27] that the radiant heat transfer from printed parts to the environment can be ignored when forced convection is anticipated in FFF. Indeed, apart from the forced convection, the low layer thickness ($h = 300 \text{ }\mu\text{m}$) also characterises this dataset. The significance of radiant heat transfer will be re-examined with other datasets.

The convection intensity can be subjected to considerable variations in FFF since (1) the part cooling fan only works in the nozzle vicinity and has directional influence; (2) the air temperature above the build plate also affects the temperature difference in Newton’s law of cooling, thus the convection flux. In Sim.2-1, the convective heat transfer coefficient h was set to $60 \text{ W/m}^2\text{/K}$ when the fan was activated and set to its maximum speed. Regarding the uncertainty in this coefficient, consider Sim.2-5 as a limiting case with $h = 8.5 \text{ W/m}^2\text{/K}$ for natural convection [23]. Sim.2-5 differs from Sim.2-1 only by h . Logically, a lower convective coefficient results in a slower cooling profile (Fig. 8b). At the same time, all other heat transfer characteristics (e.g. inter-layer and intra-layer reheating peaks locations and heights) are preserved. The $\|\bullet\|_\infty$ norm calculates that $\|T_{2.5} - T_{2.1}\|_\infty = 26 \text{ }^\circ\text{C}$, meaning that the accuracy in h can exert a significant influence on the cooling in FFF, as also reported in [7, 27]. Hence, an accurate description of the convection coefficient h under different fan working conditions and surface orientations is vital to the model accuracy.

5.2 Set 3 and the influence of temperature-dependent material properties

Set 3 includes experimental data collected in printing with a six-axis robot arm. The geometry is a single-walled square box, equivalent to a single-wall of quadruple length in heat transfers. Details in the experimental monitoring and simulations are in line with [3].

Figure 9 presents the experimental temporal temperature profile at the geometry centre (Exp.3) with different simulations. The shifted time 0 indicates the deposition moment at the location of interest. In Sim.3-1, the mass density ρ and specific heat capacity c_p took the temperature-dependent form. In contrast, the thermal conductivity λ was a constant

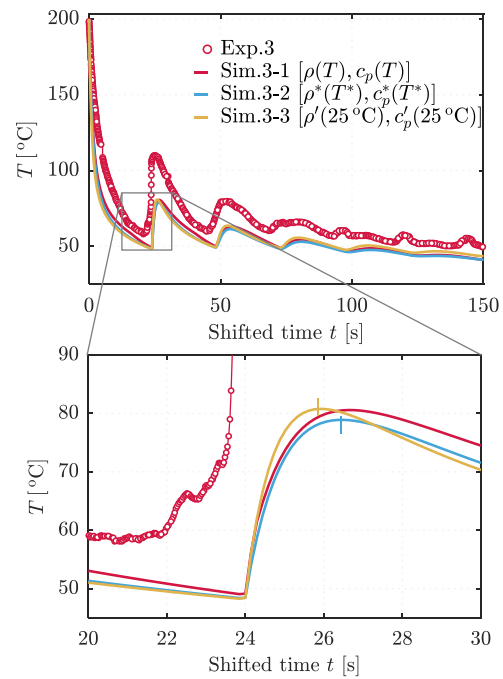


Fig. 9 [Set 3] Temperature profiles in printing the single-walled box with a robotic arm-controlled FFF, and the influence of temperature-dependent material properties

as its dependence on T is weak (Appendix 3—Fig. 15). In general, Sim.3-1 and monitoring data agree well with each other regarding the initial rapid cooling, inter-layer reheating, overall cooling, etc., despite that some discrepancies are observed.

Although both ρ and c_p strongly depend on temperature T , their product (and ultimately the thermal diffusivity α) only has a weak dependence on T , especially above T_g (Appendix 3—Fig. 15). To investigate the influence of temperature-dependent material properties, Sim.3-2 with constant $\rho^* = 1.226 \text{ g/cm}^3$ and $c_p^* = 1.801 \text{ J/g/K}$ was performed and presented in Fig. 9. These material properties were chosen based on an equivalent entropy density concept at a to-be-determined temperature T^* such that

$$\rho^*(T^*)c_p^*(T^*) = \frac{1}{T_n - T_\infty} \int_{T_\infty}^{T_n} \rho(T)c_p(T) dT.$$

With the experimental data in [44], T^* was found to be $58.11 \text{ }^\circ\text{C}$. Consequentially, ρ^* and c_p^* were determined by interpolation with the ‘pchip’ method. However, the maximum temperature difference between the simulations with dynamic and static material properties is

$$\|T_{3.2} - T_{3.1}\|_\infty = 4.4 \text{ }^\circ\text{C},$$

which is hardly discernible in Fig. 9. On the other hand, if simply taking $\rho' = 1.25 \text{ g/cm}^3$ and $c_p' = 1.314 \text{ J/g/K}$ as

the room temperature 25 °C in Sim.3-3 (the product $\rho'c'_p$ is lower than $\rho^*c_p^*$ by 26%), the profile does not significantly differ from the previous two. The maximum temperature differences are

$$\|T_{3-3} - T_{3-2}\|_{\infty} = 10 \text{ }^{\circ}\text{C},$$

$$\|T_{3-3} - T_{3-1}\|_{\infty} = 14 \text{ }^{\circ}\text{C}.$$

Hence, taking constant material properties in simulations in this article and many other publications may be justified.

Since the thermal diffusivity $\alpha = \lambda/(\rho c_p)$ is what ultimately used in the calculation, the uncertainties in ρ or c_p —in a dynamic/static form, or at the room/elevated temperature—can also be reflected in the uncertainty in λ , and vice versa. Data Set 4 sheds more light on this respect.

5.3 Set 4 and the uncertainty in thermal convection and conduction

The experimental data in Set 4 come from Lepoivre et al. [10], where a heated chamber was used. The chamber temperature was raised to reduce the convective heat flux. The temporal profile at the centre on the sixth layer in printing a single-wall is shown in Fig. 10a (Exp.4). The temperature profile decreases towards the elevated chamber temperature ($T_{\infty} = 95 \text{ }^{\circ}\text{C}$). During the cooling, only one inter-layer reheating peak is noticeable, suggesting that the heat penetration lasts for only two (or at most three) layers at an intermediate layer thickness h of 800 μm .

The simulation performed by Lepoivre et al. [10] used a different numerical scheme, where they considered the thermal contact resistance but ignored the radiant heat transfer ($\epsilon = 0$). Following the exact process parameters and material properties in [10], the T4F³ model overpredicted the cooling (Sim.4-0, Fig. 10a); however, the reheating characteristics in the profile (e.g. the reheating peak height and penetration depth) matched the monitoring data. In particular, the authors used $h = 30 \text{ W/m}^2/\text{K}$ for natural convection. Considering the uncertainty in the convection intensity, two levels of lower h were chosen and used in Sim.4-1 ($h = 15 \text{ W/m}^2/\text{K}$) and Sim.4-2 ($h = 8.5 \text{ W/m}^2/\text{K}$). Logically, the lower the value of h , the slower is the overall cooling (Fig. 10a). The profile in Sim.4-2 was substantially higher than the monitoring, but if the radiant heat transfer was considered (additionally taking $\epsilon = 0.91$), Sim.4-3 provided a better result.

As analysed, the uncertainties in material properties (ρ , c_p) and mesostructure dimensions (hypothesis H1) can be

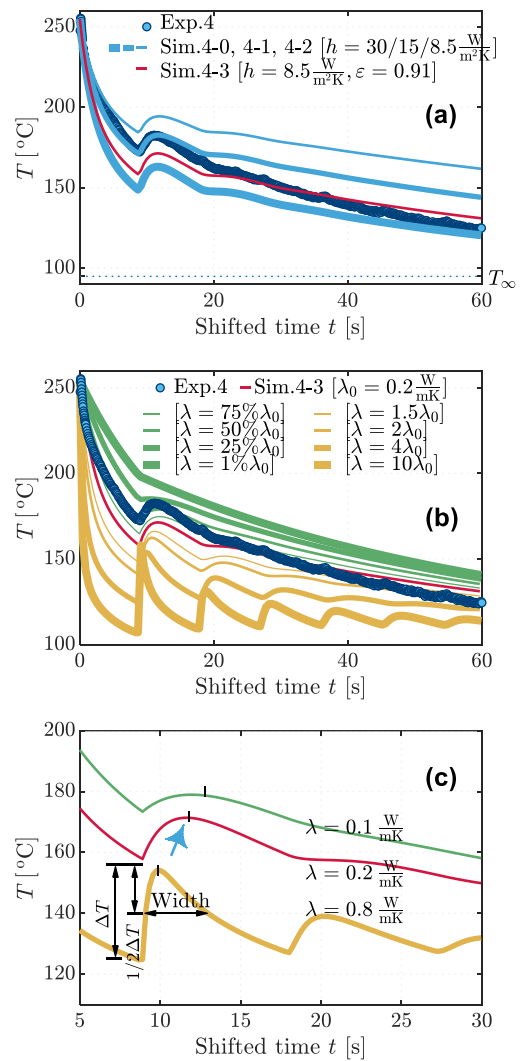


Fig. 10 [Set 4] Temperature profiles in FFF with a temperature controlled chamber. **a** The monitoring and simulations. **b**, **c** The impact of thermal conductivity λ in the simulation. (Figure reproduced based on data in [10], with permission from Elsevier.)

directly transferred to thermal conductivity λ . Thus, an effective λ for proper calculations can considerably deviate from the intrinsic material property. To investigate the impact of such uncertainty in λ on the temperature profile, Fig. 10b presents a series of simulations (based on Sim.4-3, $\lambda_0 = 0.2 \text{ W/mK}$), ranging from 1% λ_0 to 10 λ_0 . For all simulations, algorithm stability was observed. In the figure, λ is positively correlated to the cooling rate. The higher the λ , the higher is the reheating peak height, and the more pronounced is the heat penetration depth (or, the bigger is the reheating peak number). Furthermore, the magnified Fig. 10c indicates that

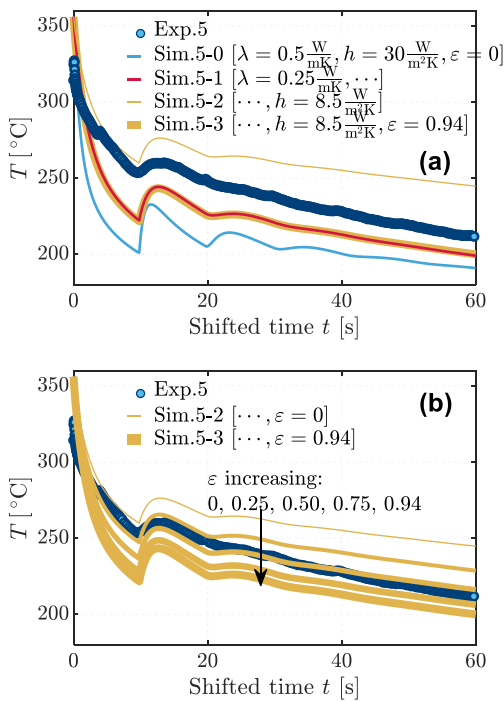


Fig. 11 [Set 5] **a** Temperature profiles in printing PEKK. **b** The role of radiant heat transfer in the simulation. (Figure reproduced based on data in [10], with permission from Elsevier.)

when λ is higher, the reheating peak width (full width at half maximum) is smaller, and intuitively, the time to reach the peak summit due to reheating is shorter. These observations are consistent with the simulations in Fig. 9, where the product ρc_p in Sim.3-3 is lower than that in Sim.3-2 by 26%, which is equivalent to a higher λ in Sim.3-3 (but with the same ρc_p). Similarly, the reheating peak is higher, and the time required to reach the peak summit is shorter in Sim.3-3.

These correlations between reheating peak characteristics and thermal conductivity can help to double check the magnitude of material properties used in simulations. One such example is given in data Set 5.

5.4 Set 5 and the uncertainty in the emissivity

Temperature data in Set 5 come from FFF with PEKK in [10], where the nozzle temperature T_n was 356 °C. The experimental temporal profile at the centre on the sixth layer in printing a single-wall is displayed in Fig. 11a (Exp.5). The maximum temperature upon deposition was not properly captured, as in Set 1.

Following the exact material properties and process parameters presented in [10] ($\lambda = 0.5 \text{ W/mK}, h = 30 \text{ W/}$

$\text{m}^2\text{/K}, \epsilon = 0$), Sim.5-0 from the T4F³ model only gave a rough prediction, with the absolute difference reaching up to 50 °C. Recalling the correlations in data Set 4 (higher λ —higher reheating peak height/number—lower peak width), all reheating characteristics in Sim.5-0 indicate that $\lambda = 0.5 \text{ W/mK}$ is excessively higher than the effective material conductivity. (The original simulation in [10] also considered the thermal contact resistance.) Hence, $\lambda = 0.25 \text{ W/mK}$ from [43] was adopted for PEKK in all further simulations. The subsequent Sim.5-1 delivered a better prediction than Sim.5-0, with slower cooling rates and a reheating peak of lower height but larger width. Furthermore, following the same choice of $h = 8.5 \text{ W/m}^2\text{/K}$ for natural convection, Sim.5-2 provided an upper bound for the monitoring. If the radiant heat transfer is additionally considered, Sim.5-3 ($\epsilon = 0.94$) delivered a lower bound for the monitoring. These results suggest that an intermediate emissivity could deliver a better simulation.

However, accurately determining the emissivity (or any other material property/process parameter) is beyond the scope of this article. Figure 11b intuitively demonstrates how the emissivity affects the temperature profiles: the higher the emissivity, the faster is the cooling and the lower the temperature approaches the steady state. Unlike the case in Set 2 where the radiant heat transfer is insignificant, radiant heat transfer in Set 5 is still essential even at a low emissivity (e.g. $\epsilon = 0.25$) when the nozzle temperature is high.

It is worthwhile to note that Sim.5-1 and Sim.5-3 give almost identical results: $\|T_{5-1} - T_{5-3}\|_\infty = 2.5 \text{ }^\circ\text{C}$. This coincident appeared because the effective heat transfer coefficient $h_{\text{eff}} \equiv h + h_{\text{rad}}$ in Sim.5-3 is higher than $h = 30 \text{ W/m}^2\text{/K}$ in Sim.5-1 at the deposition temperature; but, it decreases with the temperature during cooling. Such a coincident suggests that the radiant heat transfer somehow acts as if an additional source of thermal convection with a coefficient $h = 21.5 \text{ W/m}^2\text{/K}$ is present in this dataset. Hence, its significance during the cooling is self-explanatory. More results on the significance of radiant heat transfer are presented in Set 6.

5.5 Set 6 and the influence of resolution (or layer thickness)

Temperature data in Set 6 come from Compton et al. [23], where a BAAM system working on fused pellets was used in the printing. The BAAM system is characterised by the capability to build geometries of big dimensions (e.g. $> 1 \text{ m}^3$) at a high material flow rate (e.g. $> 10^4 \text{ cm}^3\text{/h}$) and a high

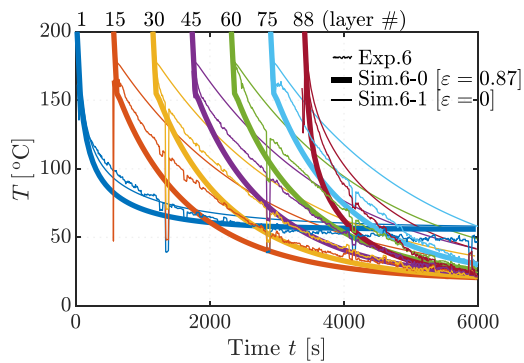


Fig. 12 [Set 6] Temperature profiles in the BAAM system at a layer thickness of 4.064 mm. (Figure reproduced based on data in [23], with permission from Elsevier.)

layer thickness (e.g. $> 1000 \mu\text{m}$. A higher layer thickness means a lower resolution). Although the BAAM system is not a fused filament technique, the processes after the material leaves the nozzle share a great similarity.

In printing a single-wall of 88 layers, the temperature profiles of a few characteristic layers were monitored and demonstrated as the noisy curves in Fig. 12 (Exp.6). It is interesting to note that the reheating peaks disappeared. This phenomenon appreciably resembles the simulations in Fig. 10b when the conductivity took only 25% or 1% of the true material properties ($\lambda = 25\% \lambda_0$, the Biot number $\text{Bi} = h\bar{h}/\lambda = 0.14$; $\lambda = 1\% \lambda_0$, $\text{Bi} = 3.4$). However, the disappearance here is due to the layer thickness \bar{h} reaching 4 mm: on the one hand, \bar{h} is comparable to the typical heat penetration depth in FFF, meaning that thermal energy cannot efficiently penetrate through such a distance; on the other, the temperature is no longer homogeneous across the layer thickness in the millimetre range. The $\text{Bi} = 0.20$ indicates that the energy transferred by conduction across adjacent layers may lose its significance to the combined effects of thermal diffusion within the strand, convection and radiation. As a result, one can only observe discontinuities in the cooling rates before and after the reheating but no longer the reheating peaks.

The Sim.6-0 took the exact material properties and process parameters as in [23]. Despite some discrepancies, all characteristics (e.g. disappearance of the reheating peak) in the temperature profiles were well simulated. Except for the first layer (which was heavily influenced by the build plate), Sim.6-0 overpredicted the cooling with a material emissivity $\varepsilon = 0.87$. However, the predictions by Sim.6-1 gave an upper

bound for the experimental monitoring when ignoring the radiant heat transfer. Logically, an intermediate emissivity can give a better prediction. In addition, its significance is self-explanatory again, even at a low-moderate nozzle temperature of $200 \text{ }^\circ\text{C}$.

6 Conclusions

This article presents a three-dimensional transient-state numerical model T4F³ for temperature fields and their variations in fused filament fabrication (FFF) printed parts. It admits at least 18 input variables among geometry dimensions, material properties and process parameters, including dynamic material properties, material anisotropy and radiant heat transfer. The model validation is performed against six sets of experimental data, covering data obtained with different machines, geometries, materials, processes, temperature measuring methods, etc. Certain discrepancies between the experimental data and simulations are observed, but they can be reasonably ascribed to the errors in experimental monitoring and uncertainties in the input variables. All critical heat transfer characteristics in the monitoring are satisfactorily simulated. The T4F³ model has been made openly available on the website <https://iiv.kuleuven.be/onderzoek/aml/technologyoffer>. During the investigations, significant insights into the thermal process of FFF are also obtained:

- A concept of heat penetration depth has been identified for FFF printing with poly(lactic acid), ranging from 2.4 to 3 mm (or 8–12 layers at a layer thickness of $300 \mu\text{m}$). Any local thermal disturbance (due to deposition, reheatings, unique thermal boundary, etc.) has little influence on locations 3 mm away.
- The reheating peaks in temporal temperature profiles are closely related to the Biot number Bi . A lower Bi —due to lower layer thickness and/or higher thermal conductivity—correlates to a higher reheating peak, a lower peak width, a shorter time to reach the summit, and a higher heat penetration depth.
- The radiant heat transfer between the printed parts and the far environment can be ignored in FFF only when printing at a medium/high-resolution (e.g. layer thickness $\bar{h} \leq 300 \mu\text{m}$) and subjected to forced convection. In all other cases, it cannot be ignored.
- Temperature-dependent material properties may not outperform constants in the heat transfer. Constant material

properties at a temperature close to the glass transition temperature are recommended for simulations.

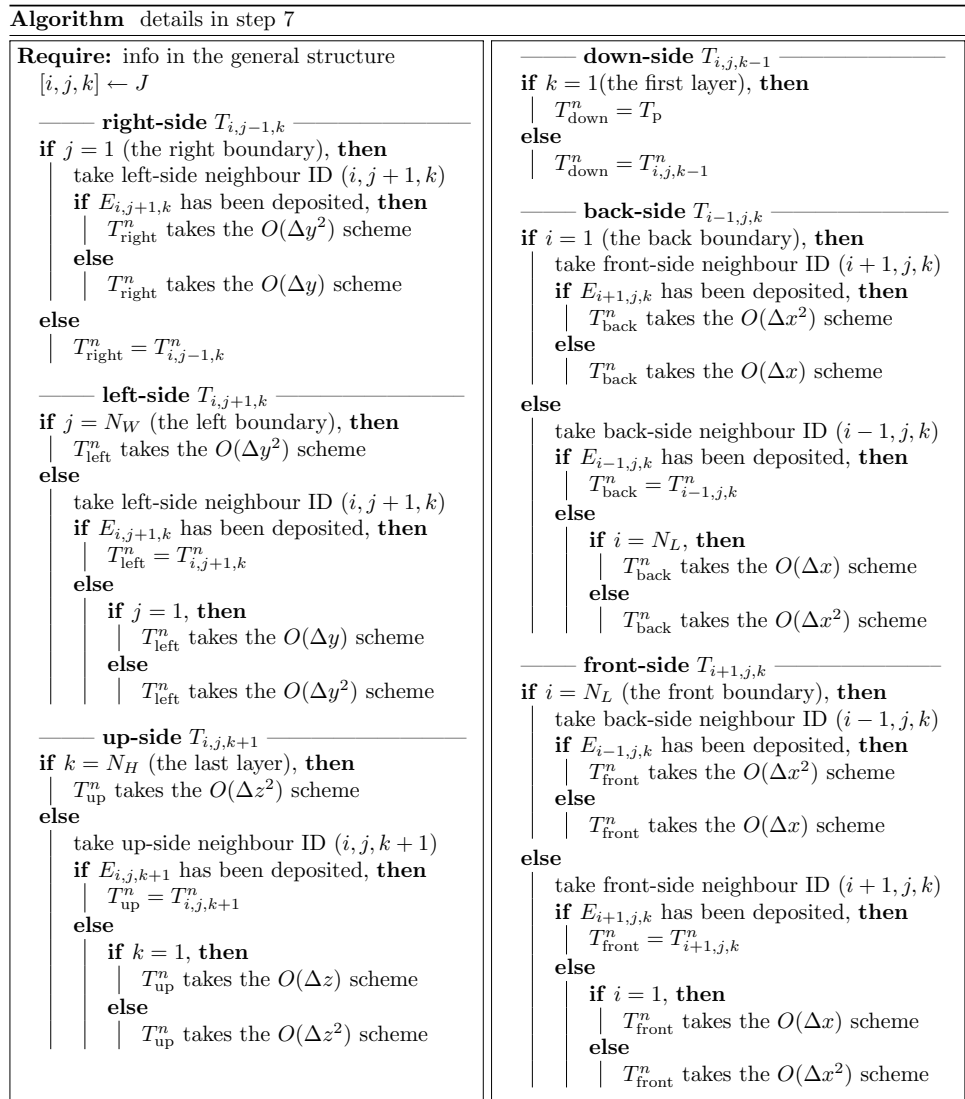
So far, the T4F³ model has been successfully applied to explain the role of a closed chamber (on the decaying air temperature $T_a(z)$ above the build plate [19]), the possibility of FFF in vacuum (on the dependence of thermal convection on the air pressure [47]), the inter-layer time similarity rule [3], etc. With minimal modifications, it can be used to quantify the effect of pre/post-heating with a hot plate attached to the nozzle [39] (on the role of a specialised form of $T_a(z)$), to study the hot-end designs [34, 36] (on the role of radiant heat transfer from the hot-end), or to study the thermal process of continuous fibre-reinforced printing [48] (on the role of conduction anisotropy), etc. It is noteworthy that the model still suffers from heavy calculation and data storage.

The simulation process may lag behind the physical process of printing. Hence, it does not suffice for online feedback control with the current single-scale geometry modelling strategy. Despite so, it establishes a firm step towards future investigations into the non-isothermal bond quality, crystallinity development (for semi-crystalline materials only), thermal deformations, etc., where reliable temperature data are the prerequisite.

T4F³ algorithm details

See Fig. 13.

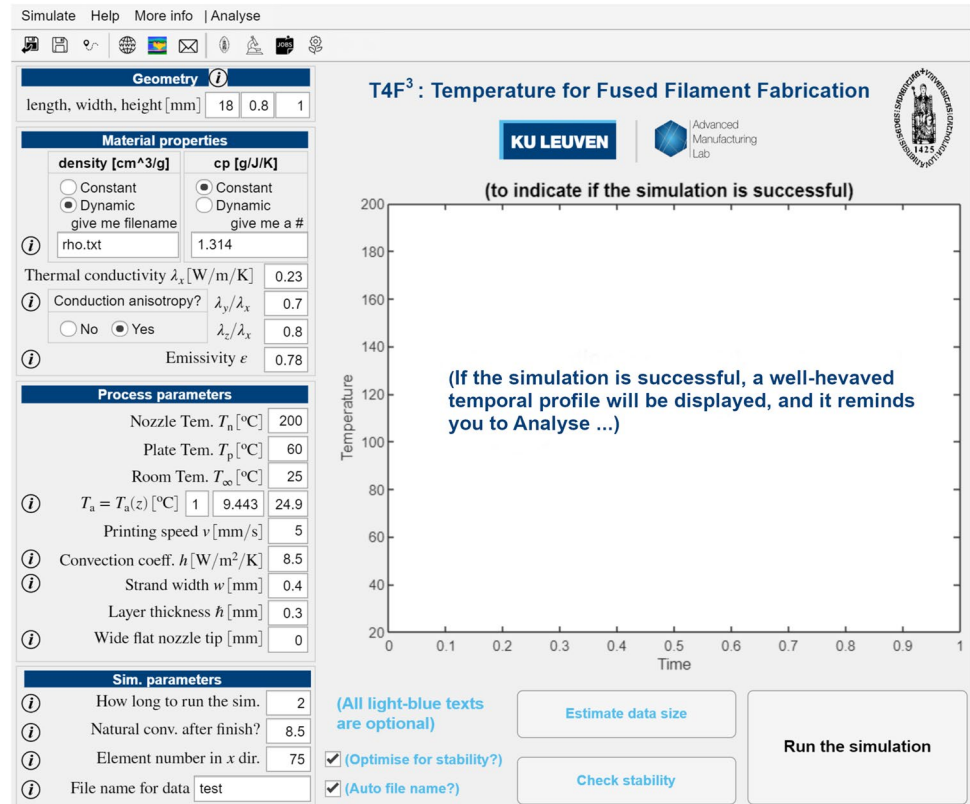
Fig. 13 Algorithm details in step 7 in the pseudocode in Fig. 3



A screenshot of the main graphic user interface of the T4F3 application

See Fig. 14.

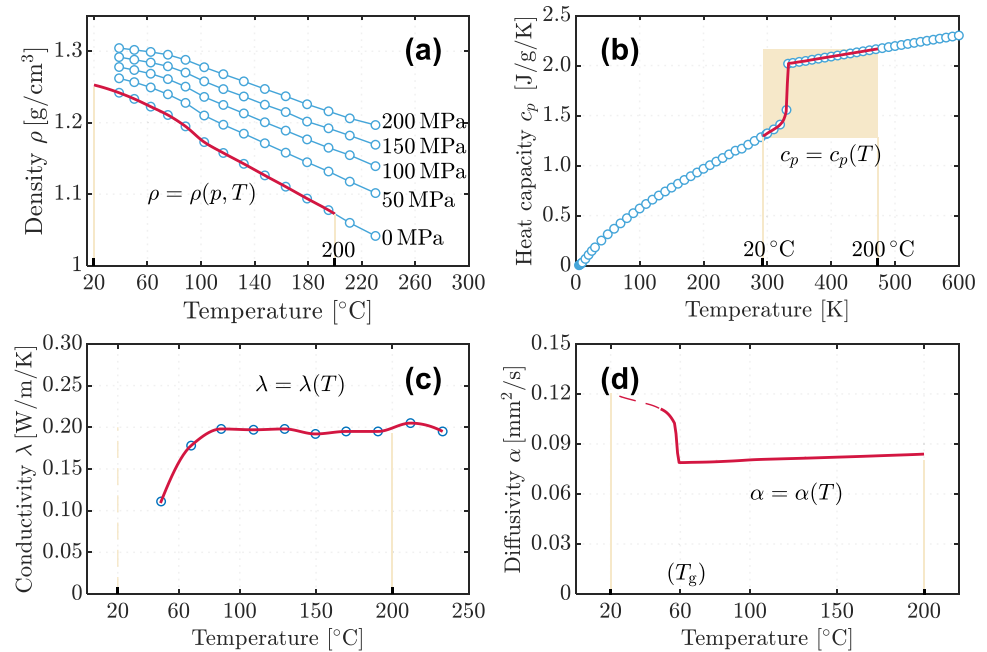
Fig. 14 The graphical user interface of the T4F³ application



Temperature-dependent material properties of PLA

See Fig. 15.

Fig. 15 **a** Mass density ρ ; **b** specific heat capacity c_p ; **c** thermal conductivity λ ; **d** thermal diffusivity $\alpha = \lambda/(\rho c_p)$. The red lines are interpolation and extrapolation results with the ‘pchip’ method based on data in [44, 45]. (Figure reproduced with permissions from Elsevier)



Acknowledgements This work was partially supported by SIM (Strategic Initiative Materials in Flanders) and VLAIO (Flemish government agency Flanders Innovation & Entrepreneurship) in the “Flaminco” project [HBC.2017.0325] and in the “RoMuPAM” project [HBC.2018.0013]. The authors would like to thank Egle Vasiliauskaite from Thomas More University of Applied Sciences for the help in acquiring dataset 3. In addition, the authors acknowledge Arthur Lepoivre from the Université de Nantes for sharing datasets 4 & 5, and Brett G. Compton from the University of Tennessee for sharing dataset 6.

Author contributions JZ: conceptualization, methodology, formal analysis, investigation, and writing—original draft. BVH: funding acquisition, writing—review and editing, project administration. EF: funding acquisition, resources, supervision, writing—review and editing, and project administration.

Availability of data and material The T4F³ model required to reproduce these findings is available on <https://iiv.kuleuven.be/onderzoek/aml/technologyoffer>. Other processed or raw data are available from the authors upon a reasonable request.

Declarations

Conflict of interest The authors declare that they have no conflict of interest.

Open Access This article is licensed under a Creative Commons Attribution 4.0 International License, which permits use, sharing, adaptation, distribution and reproduction in any medium or format, as long

as you give appropriate credit to the original author(s) and the source, provide a link to the Creative Commons licence, and indicate if changes were made. The images or other third party material in this article are included in the article's Creative Commons licence, unless indicated otherwise in a credit line to the material. If material is not included in the article's Creative Commons licence and your intended use is not permitted by statutory regulation or exceeds the permitted use, you will need to obtain permission directly from the copyright holder. To view a copy of this licence, visit <http://creativecommons.org/licenses/by/4.0/>.

References

- Hong Y, Mrinal M, Phan HS, Tran VD, Liu X, Luo C (2022) In-situ observation of the extrusion processes of Acrylonitrile Butadiene Styrene and Polylactic Acid for material extrusion additive manufacturing. *Addit Manuf* 49:102507. <https://doi.org/10.1016/j.addma.2021.102507>
- Serdeczny MP, Comminal R, Mollah MT, Pedersen DB, Spangenberg J (2020) Numerical modeling of the polymer flow through the hot-end in filament-based material extrusion additive manufacturing. *Addit Manuf* 36:101454. <https://doi.org/10.1016/j.addma.2020.101454>
- Zhang J, Vasiliauskaite E, De Kuyper A, De Schryver C, Vogeler F, Desplentere F, Ferraris E (2021) Temperature analyses in fused filament fabrication: from filament entering the hot-end to the printed parts, 3D Print. *Addit Manuf*. <https://doi.org/10.1089/3dp.2020.0339>
- Yin J, Lu C, Fu J, Huang Y, Zheng Y (2018) Interfacial bonding during multi-material fused deposition modeling (FDM) process

- due to inter-molecular diffusion. *Mater Des* 150:104–112. <https://doi.org/10.1016/j.matdes.2018.04.029>
5. Lepoivre A, Levy A, Boyard N, Gaudefroy V, Sobotka V (2021) Coalescence in fused filament fabrication process: thermo-dependent characterization of high-performance polymer properties. *Polym Test* 98:107096. <https://doi.org/10.1016/j.polymertesting.2021.107096>
 6. Sun Q, Rizvi GM, Bellehumeur CT, Gu P (2008) Effect of processing conditions on the bonding quality of FDM polymer filaments. *Rapid Prototyp J* 14:72–80. <https://doi.org/10.1108/13552540810862028>
 7. Vanaei HR, Shirinbayan M, Costa SF, Duarte FM, Covas JA, Deligant M, Khelladi S, Tcharkhtchi A (2020) Experimental study of PLA thermal behavior during fused filament fabrication. *J Appl Polym Sci*. <https://doi.org/10.1002/app.49747>
 8. Kousiatza C, Karalekas D (2016) In-situ monitoring of strain and temperature distributions during fused deposition modeling process. *Mater Des* 97:400–406. <https://doi.org/10.1016/j.matdes.2016.02.099>
 9. Ferraris E, Zhang J, Van Hooreweder B (2019) Thermography based in-process monitoring of Fused Filament Fabrication of polymeric parts. *CIRP Ann* 68:213–216. <https://doi.org/10.1016/j.cirp.2019.04.123>
 10. Lepoivre A, Boyard N, Levy A, Sobotka V (2020) Heat transfer and adhesion study for the FFF additive manufacturing process. *Proc Manuf*. <https://doi.org/10.1016/j.promfg.2020.04.291>
 11. Oleff A, Küster B, Stonis M, Overmeyer L (2021) Process monitoring for material extrusion additive manufacturing: a state-of-the-art review. *Prog Addit Manuf*. <https://doi.org/10.1007/s40964-021-00192-4>
 12. Gleadall A, Ashcroft I, Segal J (2018) VOLCO: A predictive model for 3D printed microarchitecture. *Addit Manuf* 21:605–618. <https://doi.org/10.1016/j.addma.2018.04.004>
 13. El Moumen A, Tarfaoui M, Lafdi K (2019) Modelling of the temperature and residual stress fields during 3D printing of polymer composites. *Int J Adv Manuf Technol* 104:1661–1676. <https://doi.org/10.1007/s00170-019-03965-y>
 14. Manikandan N, Vignesh T, Prasath C, Ismail M (2020) Thermo-Mechanical analysis of fused filament fabrication process. *IOP Conf Ser Mater Sci Eng*. <https://doi.org/10.1088/1757-899X/764/1/012008>
 15. Das A, McIlroy C, Bortner MJ (2020) Advances in modeling transport phenomena in material-extrusion additive manufacturing: Coupling momentum, heat, and mass transfer. *Prog Addit Manuf*. <https://doi.org/10.1007/s40964-020-00137-3>
 16. Zhang J, Wang X, Yu W, Deng Y (2017) Numerical investigation of the influence of process conditions on the temperature variation in fused deposition modeling. *Mater Des* 130:59–68. <https://doi.org/10.1016/j.matdes.2017.05.040>
 17. Zhang Y, Shapiro V (2017) Linear time thermal simulation of FDM process. *Proc ASME Des Eng Tech Conf*. <https://doi.org/10.1115/DETC2017-68293>
 18. Afrasiabi M, Lüthi C, Bambach M, Wegener K (2021) Multi-resolution SPH simulation of a laser powder bed fusion additive manufacturing process. *Appl Sci*. <https://doi.org/10.3390/app11072962>
 19. Zhang J, Van Hooreweder B, Ferraris E (2021) Measurement, characterisation and influence of the air temperature above the build plate in fused filament fabrication. *Addit Manuf Lett*. <https://doi.org/10.1016/j.addlet.2021.100013>
 20. Luo C, Wang X, Migler KB, Seppala JE (2020) Effects of feed rates on temperature profiles and feed forces in material extrusion additive manufacturing. *Addit Manuf* 35:101361. <https://doi.org/10.1016/j.addma.2020.101361>
 21. McIlroy C, Olmsted PD (2017) Deformation of an amorphous polymer during the fused-filament-fabrication method for additive manufacturing. *J Rheol (NY)* 61:379–397. <https://doi.org/10.1122/1.4976839>
 22. Whyman S, Arif KM, Potgieter J (2018) Design and development of an extrusion system for 3D printing biopolymer pellets. *Int J Adv Manuf Technol* 96:3417–3428. <https://doi.org/10.1007/s00170-018-1843-y>
 23. Compton BG, Post BK, Duty CE, Love L, Kunc V (2017) Thermal analysis of additive manufacturing of large-scale thermoplastic polymer composites. *Addit Manuf* 17:77–86. <https://doi.org/10.1016/j.addma.2017.07.006>
 24. Klein J, Stern M, Franchin G, Kayser M, Inamura C, Dave S, Weaver JC, Houk P, Colombo P, Yang M, Oxman N (2015) Additive manufacturing of optically transparent glass. *3D Print. Addit Manuf* 2:92–105. <https://doi.org/10.1089/3dp.2015.0021>
 25. Inamura C, Stern M, Lizardo D, Houk P, Oxman N (2018) Additive manufacturing of transparent glass structures. *3D Print. Addit Manuf* 5:269–283. <https://doi.org/10.1089/3dp.2018.0157>
 26. Leung PYV (2017) Sugar 3D printing: Additive manufacturing with molten sugar for investigating molten material fed printing. *3D Print. Addit Manuf* 4:13–17. <https://doi.org/10.1089/3dp.2016.0045>
 27. Costa SF, Duarte FM, Covas JA (2015) Thermal conditions affecting heat transfer in FDM/FFE: a contribution towards the numerical modelling of the process: This paper investigates convection, conduction and radiation phenomena in the filament deposition process. *Virtual Phys Prototyp* 10:35–46. <https://doi.org/10.1080/17452759.2014.984042>
 28. Prajapati H, Ravoori D, Woods RL, Jain A (2018) Measurement of anisotropic thermal conductivity and inter-layer thermal contact resistance in polymer fused deposition modeling (FDM). *Addit Manuf* 21:84–90. <https://doi.org/10.1016/j.addma.2018.02.019>
 29. Elkholy A, Rouby M, Kempers R (2019) Characterization of the anisotropic thermal conductivity of additively manufactured components by fused filament fabrication. *Prog Addit Manuf* 4:497–515. <https://doi.org/10.1007/s40964-019-00098-2>
 30. Quiroga Cortés L, Caussé N, Dantras E, Lonjon A, Lacabanne C (2016) Morphology and dynamical mechanical properties of poly ether ketone ketone (PEKK) with meta phenyl links. *J Appl Polym Sci* 133:1–10. <https://doi.org/10.1002/app.43396>
 31. Yu W, Wang X, Ferraris E, Zhang J (2019) Melt crystallization of PLA/Talc in fused filament fabrication. *Mater Des*. <https://doi.org/10.1016/j.matdes.2019.108013>
 32. Mazzullo S, Paganetto G, Celli A (1992) Regime III crystallization in poly-(L-lactic) acid. *Prog Colloid Polym Sci* 34:32–34. <https://doi.org/10.1007/BFb0115570>
 33. da Cunha Vasconcelos G, Mazur RL, Botelho EC, Rezende MC, Costa ML (2010) Evaluation of crystallization kinetics of poly(ether-ketone-ketone) and poly(ether-ether-ketone) by DSC. *J Aerosp Technol Manag* 2:155–162. <https://doi.org/10.5028/jatm.2010.02026310>
 34. Thézé A, Régnier G, Guinault A, Richard S, Macquaire B (2021) Fused filament fabrication printing process of polymers highly filled with metallic powder: a significant influence of the nozzle radiation on the substrate temperature. *Int J Mater Form*. <https://doi.org/10.1007/s12289-021-01645-5>
 35. Seppala JE, Migler KD (2016) Infrared thermography of welding zones produced by polymer extrusion additive manufacturing. *Addit Manuf* 12:71–76. <https://doi.org/10.1016/j.addma.2016.06.007>

36. Hu B, Duan X, Xing Z, Xu Z, Du C, Zhou H, Chen R, Shan B (2019) Improved design of fused deposition modeling equipment for 3D printing of high-performance PEEK parts. *Mech Mater* 137:103139. <https://doi.org/10.1016/j.mechmat.2019.103139>
37. Kishore V, Ajinjeru C, Nycz A, Post B, Lindahl J, Kunc V, Duty C (2017) Infrared preheating to improve interlayer strength of big area additive manufacturing (BAAM) components. *Addit Manuf* 14:7–12. <https://doi.org/10.1016/j.addma.2016.11.008>
38. Ravoori D, Prajapati H, Talluru V, Adnan A, Jain A (2019) Nozzle-integrated pre-deposition and post-deposition heating of previously deposited layers in polymer extrusion based additive manufacturing. *Addit Manuf* 28:719–726. <https://doi.org/10.1016/j.addma.2019.06.006>
39. Yu N, Sun X, Wang Z, Zhang D, Li J (2021) Effects of auxiliary heat on the interlayer bonds and mechanical performance of polylactide manufactured through fused deposition modeling. *Polym Test* 104:107390. <https://doi.org/10.1016/j.polymertesting.2021.107390>
40. Evans G, Blackledge J, Yardley P (2000) Numerical methods for partial differential equations. Springer, London. https://doi.org/10.1007/978-1-4471-0377-6_2
41. Advanced Manufacturing Lab, T4F3: Temperature for Fused Filament Fabrication (2021) <https://iiv.kuleuven.be/onderzoek/aml/technologyoffer>. Accessed 13 Dec 2021
42. Serdeczny MP, Comminal R, Pedersen DB, Spangenberg J (2020) Experimental and analytical study of the polymer melt flow through the hot-end in material extrusion additive manufacturing. *Addit Manuf* 32:100997. <https://doi.org/10.1016/j.addma.2019.100997>
43. Coulson M, Dantras E, Olivier P, Gleizes N, Lacabanne C (2019) Thermal conductivity and diffusivity of carbon-reinforced polyetherketoneketone composites. *J Appl Polym Sci* 136:1–8. <https://doi.org/10.1002/app.47975>
44. Sin LT, Rahmat AR, Rahman WAWA (2012) Thermal properties of poly(Lactic Acid) In: *Poly(lactic acid) PLA Biopolym. Technol. Appl.*, (Chapter 3). William Andrew, pp 109–141. doi: <https://doi.org/10.1016/B978-1-4377-4459-0.00003-2>
45. Pyda M, Bopp RC, Wunderlich B (2004) Heat capacity of poly(lactic acid). *J Chem Thermodyn* 36:731–742. <https://doi.org/10.1016/j.jct.2004.05.003>
46. Pigeonneau F, Xu D, Vincent M, Agassant JF (2020) Heating and flow computations of an amorphous polymer in the liquefier of a material extrusion 3D printer. *Addit Manuf*. <https://doi.org/10.1016/j.addma.2019.101001>
47. Zhang J, Van Hooreweder B, Ferraris E (2022) Fused filament fabrication on the Moon. *JOM*. <https://doi.org/10.1007/s11837-021-05031-z>
48. Fan C, Shan Z, Zou G, Zhan L, Yan D (2021) Interfacial bonding mechanism and mechanical performance of continuous fiber reinforced composites in additive manufacturing. *Chinese J Mech Eng*. <https://doi.org/10.1186/s10033-021-00538-7>